UCTEA Chamber of Geophysical Engineers of TURKEY
Society of Exploration Geophysicists
INTERNATIONAL GEOPHYSICAL CONFERENCE AND OIL & GAS EXHIBITION
ISTANBUL 2012

Subwavelength imaging using seismic scanning tunneling macroscope: Field data example

Gaurav Dutta, Abdullah AlTheyab, Sherif Hanafy and Gerard T. Schuster, King Abdullah University of Science and Technology*

Summary

We present the first results for a controlled source seismic experiment where we demonstrate that subwavelength scatterers can be imaged with a resolution of λ/8 using seismic data recorded in the far field of the scatterer. Using the Time Reverse Mirror (TRM) operation, we show that an image resolution Δx of 0.6 *m* can be obtained at the source location from data with seismic wavelengths ≥ 5 *m*. In other words, we show that it is possible to extract 220 *Hz* information from 55 *Hz* data using the TRM operation. These results also validate the theory of seismic superresolution associated with a seismic scanning tunneling macroscope.

Introduction

For a conventional optical lens, the resolution limit for imaging an object is governed by the Rayleigh resolution limit, $\Delta\theta=1.22\lambda/D$, where θ is the angle between the object and the optical axis of the lens. The Abbe resolution limit or the diffraction-limited image resolution is restricted to $\lambda/2$ for objects in the near field of the lens. The finer details of the object less than $\lambda/2$ are permanently lost in the image because of this fundamental diffraction limit. This loss can be attributed to the fact that the energy of the evanescent waves emitted from such fine features of the object decay exponentially away from the object and are not carried away by the propagating waves. Subwavelength optical imaging can be done if this evanescent energy is used as shown by de Fornel (2001) and Jia et al. (2010).

Recently, Schuster et al. (2012) proposed the theory for a Seismic Scanning Tunneling Macroscope (SSTM) and characterized the distribution of scatterers in a medium using synthetic examples. Their field data results with the Arizona mine tunnel experiment were however not conclusive since they could not verify the presence of subwavelength scatterers in the tunnel walls. In this paper, we present the first results of a controlled source seismic experiment where we used the TRM operation proposed by Fink (1993) on seismic data collected in the far field of the scatterer to accurately image sub-wavelength scatterers located in the near field of the source. The precise location of the scatterer is known in our experiment and hence we can authoritatively verify our results with the ground-truth. We also show that in spite of using seismic data with wavelengths ≥ 5 *m*, we can resolve finer details of the image with a resolution of 0.6 *m*.

Theory of Seismic Scanning Tunneling Macroscope

Considering the geometry shown in Figure 1 and the Green's function notation, $G(g|s)$ for a source at s and a receiver at g, for a line of sources, $s \varepsilon B_s$, and a line of receivers, $g \varepsilon B_g$, the scattered data for a point source at s and a receiver at g is given by

$$G(g \mid s) = G(g \mid s_0)G(s_0 \mid s), \qquad (1)$$

For a band-limited source spectrum between $-\omega_0$ and $+\omega_0$ and a recording aperture 2L wide, the TRM image or the post-stack migration profile (Schuster (2009)) for the point source at $s' \varepsilon B_s$ and a line of geophones along B_g is given by

$$m(s', s_0) = k. \int_{-\omega_0}^{+\omega_0} \int_{-L}^{+L} G(g \mid s_0)G(s_0 \mid s)G(g \mid s_0)^* G(s_0 \mid s')^* dg d\omega. \qquad (2)$$

On plugging the Green's function representation $G(g|s)=e^{i\omega|g-s|}/|g-s|$ in equation 2, we get

$$m(s', s_0) = \int_{-\omega_0}^{+\omega_0} \frac{e^{i\omega\left(|s_0 - s| - |s_0 - s'|\right)/c}}{|s - s_0||s' - s_0|} d\omega \int_{-L}^{L} \frac{1}{|g - s_0|^2} dg,$$

$$m(s', s_0) = \frac{\alpha \sin\left(\omega_0 \left[|s_0 - s| - |s_0 - s'|\right]/c\right)}{\left[|s_0 - s| - |s_0 - s'|\right]}, \qquad (3)$$

where α is the superresolution factor given by

$$\alpha = \frac{c}{|s - s_0||s_0 - s'|} \int_{-L}^{L} \frac{1}{|g - s_0|^2} dg.$$

It should be noted here that α is independent of the source frequency and is dependent solely on the source-scatterer and receiver-scatterer separation. The Abbe resolution limit is controlled by the sinc function in equation 3 whereas α controls the superresolution factor. According to Schuster et al. (2012), there will be enormous changes in the migration image $m(s',s_0)$ if s is near the scatterer location s_0.

Equation 2 however assumes a uniform source strength and geophone response. In field data, both of these assumptions are violated. One has to account for these variations in the TRM equation 2. We account for this variability by normalizing the shot-gathers and the windowed traces to their norm. In the field data, the windowed traces include predominantly the first arrival and the energy that arrived within $3T_0$, where T_0 is the dominant period of the arrivals. We include a variable geophone response β_g, and an indeterminate source amplitude W_s to our TRM equation 2 as

$$m(s', s_0)^{norm} = k \int_{-\omega_0}^{+\omega_0} \int_{-L}^{+L} |W_s||W_{s'}|\left|\beta_g\right|^2 G(g \mid s_0)G(s_0 \mid s)$$

$$G(g \mid s_0)^* G(s_0 \mid s')^* \gamma(s, g)\gamma(s', g) dg d\omega, \qquad (4)$$

where $\gamma(s,g)$ is designed to compensate for W_s and β_g. This normalization factor γ can be obtained by assigning it to be the scaled reciprocal of the measured amplitude of the direct arrival in the windowed trace. In other words,

$$\gamma(s,g) = \frac{1}{\left|W_s\right|\left|\beta_g\right|\left|G(g \mid s)^{direct}\right|},$$

where $G(g|s)^{direct}$ is the magnitude spectrum of the direct arrival recorded at g, the L_2 norm is assumed, and the direct arrival is assumed to be the dominant one in the windowed trace. The norm of the Green's function $||G(g|s)||^{direct} \approx 1/|s\text{-}g|$, where $|s\text{-}g|$ is the source-geophone distance. On substituting these terms in equation 4 we end up with the normalized TRM equation,

$$m(s',s_0)^{norm} = k\int_{-\omega_0}^{+\omega_0}\int_{-L}^{+L} G(g \mid s_0)G(s_0 \mid s)G(g \mid s_0)^{*}G(s_0 \mid s')^{*} \left|s-g\right|\left|s'-g\right| dg\,d\omega,$$

$$= k\frac{\alpha_1(s,s_0,s')\sin(\omega_0\left[\left|s_0-s\right|-\left|s_0-s'\right|\right])}{\left[\left|s_0-s\right|-\left|s_0-s'\right|\right]}, \quad (5)$$

where $\alpha_1(s,s_0,s')$ is the compensated superresolution factor given by

$$\alpha_1(s,s_0,s') = \frac{c}{\left|s-s_0\right|\left|s'-s_0\right|}\int_{-L}^{+L}\frac{\left|s-g\right|\left|s'-g\right|}{\left|g-s_0\right|^2}dg,$$

The factor $|s\text{-}g||s'\text{-}g|$ is a smoothly varying factor w.r.t to s', more smooth than the sinc function in equation 5. Thus, normalizing the shot gathers for the field experiment does not affect the superresolution factor in this case.

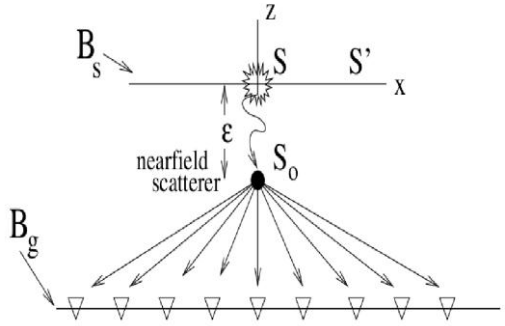

Figure 1: Single scatterer in the near field of the source with geophones in the far-field region (Schuster et al. 2012).

KAUST Field Experiment

Figure 2 shows the acquisition geometry for the KAUST field experiment while Figure 3 shows the set-up in the field for validating the theory of superresolution. There are 5 receiver lines, each line having 24 geophones with a receiver interval of 0.2 *m* for the nearest 3 receiver lines and 0.5 *m* for the farthest 2 lines. The 5 receiver lines are spaced at 1 *m*, 1 *m*, 5 *m* and 10 *m* from each other. The source line is at a distance of 1 *m* from the nearest

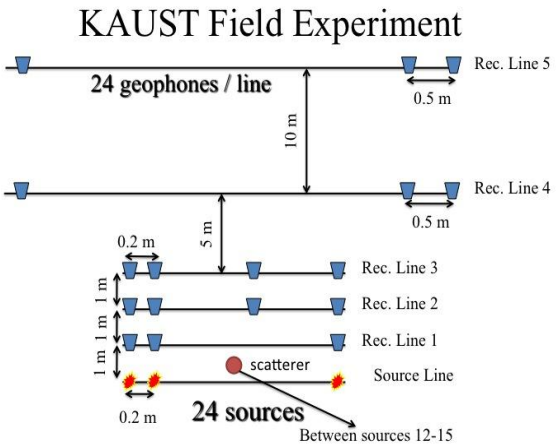

Figure 2: Layout of the Field Experiment.

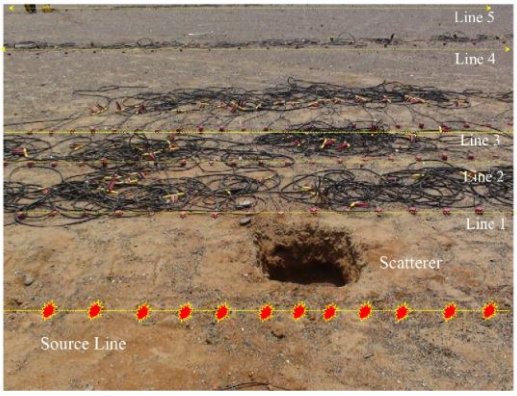

Figure 3: Experiment set-up in the field showing the scatterer location.

receiver line and there are 24 shots with a shot interval of 0.2 *m*. A 2-lb hammer is used to strike a small rectangular plate of dimensions 0.1×0.1×0.01 m^3. The experiment is conducted in two phases: phase I when there is no scatterer and phase II when a hole of dimensions 0.5×0.5×0.5 m^3 is dug into the ground which acts as the scatterer in our case (see Figure 3). The experiment is carried out in two phases with the intention of subtracting out the direct arrivals using the data in phase I and II, thereby having only the response of the scatterer left in our data. Thus, there are two sets of common shot gathers (CSGs) at each source location – one having scattered arrivals and one without. Each data set is further divided into two groups of 5 stacks each to avoid false superresolution signatures due to random noise. After correcting for some static shifts, they are normalized to account for source strength variations and geophone response variations as described in equation 4 and then stacked to give the stacked shot gather $d(g,t|s,0)^{pre}$ The same procedure is repeated for phase II of the experiment to give the stacked shot gather $d(g,t|s,0)^{post}$. Here the superscripts *pre* and *post* are used to indicate the data sets before and after putting the scatterer respectively. Figure 4 represents one such CSG from each phase of the experiment.

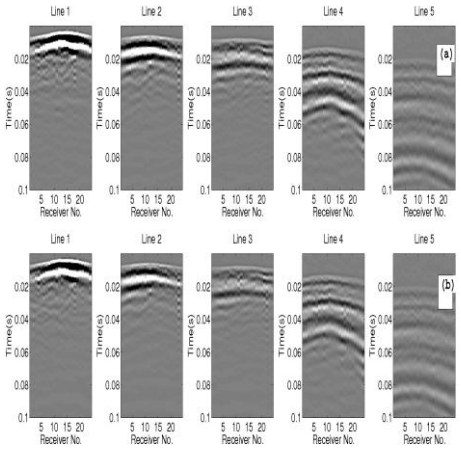

Figure 4: CSGs a) before and b) after the scatterer is buried.

The CSGs, $d(g,t|s,0)^{pre}$ and $d(g,t|s,0)^{post}$ are then subtracted to give the scattered arrivals $\Delta d(g,t|s,0) = d(g,t|s,0)^{pre} - d(g,t|s,0)^{post}$ as shown in Figure 5. This scattered data $\Delta d(g,t|s,0)$ is then used to image the source location and also to detect the scatterer at sub-wavelength resolution using the normalized TRM equation 4 to get the TRM image $m(s',s_0)$. Figure 6 summarizes the processing workflow used to get the TRM image.

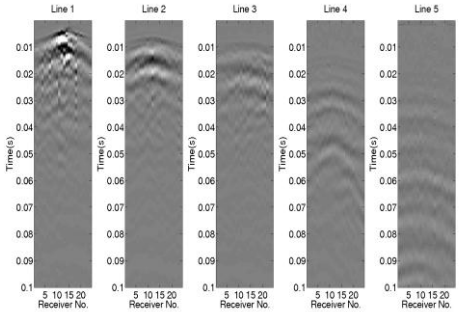

Figure 5: CSGs after subtracting the CSGs in Figure 4(a) from the corresponding ones in Figure 4(b).

Results

Figure 7 compares the TRM images before and after burying the scatterer. The hottest color in these images corresponds to the profile's peak value while the cooler colors represent the smaller values in the TRM profile. As predicted by theory in Schuster et al. (2012), the peak value is at shot location 12 (s = 12 m) which is next to the scatterer (the empty hole in this case). The TRM profile for this source location shown in Figure 8 indicates a resolution Δx = 0.6 m which is approximately equal to $\lambda_{min}/4$. On comparison with the source wavelength of ≈ 2.5 m, we can see a superresolution signature due to the near field scattering from the empty hole.

The dominant frequency content of the data is estimated to be around 110 Hz. This is estimated from the direct arrivals in the data. To validate our results, we apply a 0-55 Hz low-pass filter to the CSGs, thereby increasing the λ_{min} in the data to ≈ 5 m. The TRM operation shown in Figure 6 is then applied to the subtracted CSGs. Figure 9 compares the TRM profiles at the scatterer location from the data with and without the scattered arrivals. As expected, on reducing the bandwidth of the data, the wavelength of the data without the scatterer increased. However, the resolution obtained from the data with the

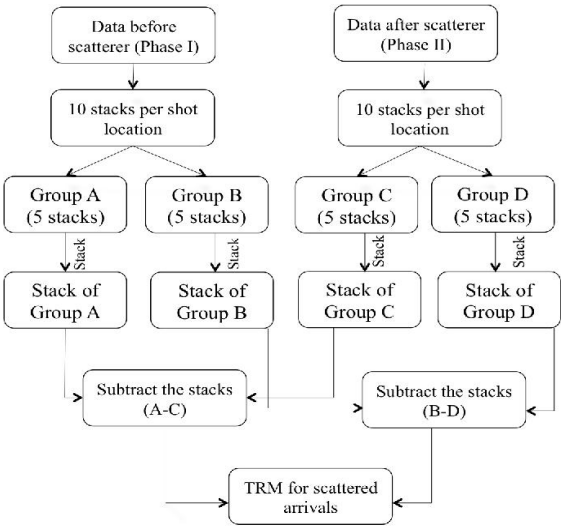

Figure 6: Flowchart for the TRM operation on the field data.

scattered arrivals remains the same (Δx = 0.6 m). Equivalently, we can say that we have extracted 220 Hz information from 55 Hz data with a spatial resolution of $\lambda/8$ in this case. The resolution from the scattered arrivals does not change even on decreasing the bandwidth of the data. This is because the width of the TRM profile is independent of the wavelength if the scatterer is in the near-field of the source as predicted by Schuster et al. (2012) in equation 3.

Conclusions

Our results with the field experiment prove that we can achieve superresolution or sub-wavelength resolution (better than $\lambda/2$) in our migration images using TRM if the scatterer lies in the near field of the source and is sub-wavelength in dimension. By reciprocity, we can also claim that if the scatterer is in the near field of the receivers, the same will hold true. However, the main challenge in achieving sub-wavelength resolution is the ability to separate out the scattered arrivals from the direct arrivals, the surface waves or any other ambient noise either through direct subtraction of using a simple window function. Also reproducing the same source signature at different source locations to get a good subtraction of the direct arrivals is a big challenge in itself.

Our future works will focus on reproducing the results of this experiment with a new field data set. Other attempts will be made to find out if the TRM methodology is capable of resolving two closely spaced sub-wavelength scatterers in the near field of the source. Also attempts will be made to identify the potential applications of

SSTM in determining sharp lithological boundaries, finding cracks in the borehole in a VSP survey or on a more global scale, determining the roughness of the subducting beds in subduction zones using local earthquake records

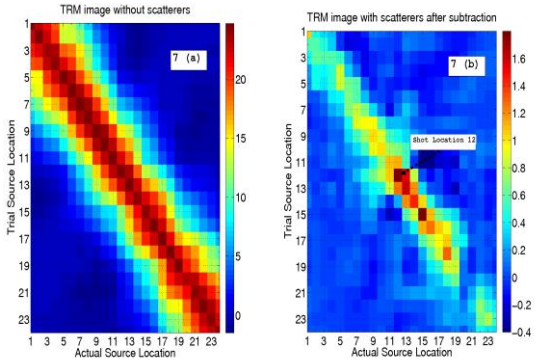

Figure 7: a) TRM image before burying a scatterer. The high correlation values are seen along the diagonal since each shot gets correlated with itself. b) TRM image after burying a scatterer and subtracting out the direct arrivals. The highest correlation value is at source location 12 which is next to the scatterer.

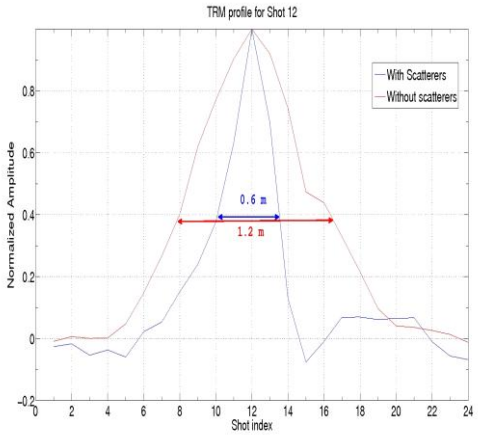

Figure 8: TRM profile for shot 12 showing superresolution at the source location. The blue curve represents the resolution obtained using the scattered only wavefield while the red curve shows the resolution without the scattered wavefield. The half-width of the blue curve is 0.6 *m* indicating a sub-wavelength resolution of approximately λ/4.

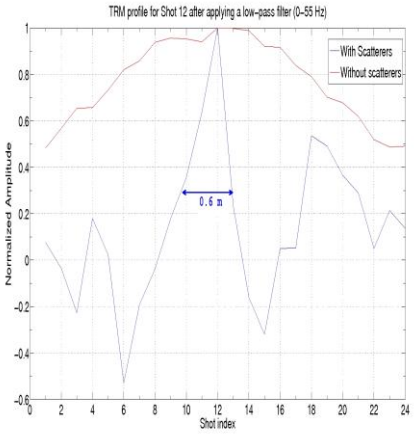

Figure 9: TRM profile for shot 12 after applying a bandpass filter of 0-55 *Hz*. The blue curve represents the resolution obtained using the scattered only wavefield while the red curve shows the resolution without the scattered wavefield. The resolution of the blue curve did not change after applying a low pass filter to the data since it is dependent only on the source-scatterer separation.

Acknowledgements

We are grateful to KAUST and all the sponsors of the Center for Subsurface Imaging and Modeling (CSIM) consortium for providing us all the facilities and financial support required for carrying out this work.

References

de Fornel, F., 2001, Evanescent waves: from Newtonian optics to atomic optics , volume **73**: Springer Verlag.

Fink, M., 1993, Time-reverse mirrors: Journal of Physics D: Applied Physics, **26**, 1333.

Jia, H., Ke, M., Hao, R., Ye, Y., Liu, F., & Liu, Z., 2010, Subwavelength imaging by a simple planar acoustic superlens: Applied Physics Letters, **97**, 173507-173507.

Schuster, G., 2009, Seismic Interferometry: Cambridge Press.

Schuster, G., Hanafy, S., and Huang, Y., 2012, Theory and feasibility tests for a seismic scanning tunneling macroscope: Geophysics Journal International (in press).